AIAA JOURNAL
Vol. 49, No. 10, October 2011

Flutter and Stall Flutter of a Rectangular Wing in a Wind Tunnel

Norizham Abdul Razak,* Thomas Andrianne,† and Grigorios Dimitriadis‡
University of Liège, 4000 Liège, Belgium

DOI: 10.2514/1.J051041

The aeroelastic behavior of a rectangular wing with pitch and plunge degrees of freedom was observed experimentally using pressure, acceleration, and particle image velocimetry measurements. The wing was set at different static angles of attack and wind-tunnel airspeeds. The wing's dynamic behavior was governed by a two-parameter bifurcation from steady to limit cycle oscillations, with the two parameters being the airspeed and the static angle of attack. At the lowest static angle, the wing underwent a classical flutter phenomenon that was transformed into a supercritical Hopf bifurcation at higher angles. The latter was combined with a fold bifurcation at intermediate angles of attack. All limit cycle oscillations observed were either low-amplitude oscillations with time-varying amplitude or high-amplitude oscillations with nearly steady amplitude. They were caused by two different types of dynamic stall phenomena. During low-amplitude limit cycle oscillations the periodically stalled flow covered only the rear part of the wing. During high-amplitude limit cycle oscillations, trailing-edge and leading-edge separation occurred. Trailing-edge separation was characterized by a significant amount of unsteadiness, varying visibly from cycle to cycle. The occurrence of leading-edge separation was much more regular and had the tendency to stabilize the amplitude of the limit cycle oscillation motion.

I. Introduction

THE existence of nonlinearity in aeroelastic systems is known to significantly affect their dynamic behavior, sometimes causing oscillations that cannot be predicted by linear theory. One such type of oscillation is the aeroelastic phenomenon known as *stall flutter*. Traditionally, aeroelastic phenomena are considered to be dynamic response phenomena resulting from the interaction of structural, inertial, and aerodynamic forces. Such interactions can lead to the well-known phenomenon of classical linear flutter, a catastrophic self-excited oscillation. However, several other phenomena can arise from low-speed aeroelastic interactions, such as stall flutter and galloping, which are due to nonlinearity in the aerodynamic forces and lead to limit cycle oscillations (LCOs). LCOs can also occur due to the presence of other sources of nonlinearity, such as structural or material nonlinearities.

Stall flutter is a phenomenon that occurs when the flow separates from and reattaches to the surface of the wing in a cyclic manner. The separation can be partial or complete over the entire wing's surface. Flow separation is also involved in other aeroelastic phenomena, such as galloping. To differentiate between the two, it must be observed that stall flutter involves an alternation between stalled and attached flow over wings, whereas galloping involves only separated flow over bluff bodies. This alternation between stalled and attached flow is known as *dynamic stall*, a phenomenon that has been the subject of numerous experimental and theoretical investigations (see, for example, McCroskey et al. [1], Ericsson and Reding [2], and Spentzos et al. [3]).

Stall flutter itself is the result of the coupling of the vibration characteristics of a flexible structure with dynamic stall [4]. Research in the phenomenon started during World War II [5,6]. In the postwar era, Halfman et al. [7] and Rainey [8] characterized stall flutter as a motion that involves primarily torsional vibrations; it is associated with a severe drop in the critical flutter speed and the flutter frequency approaches the value of the pitching frequency at the flutter airspeed. Furthermore, stall flutter can be significantly influenced by the occurrence of static divergence [9,10]. The stall-flutter phenomenon has been encountered in helicopter rotor blades [11], wind turbine blades, low-stiffness wings operating at high angles of attack, and wind-tunnel models [12].

Stall flutter is essentially a limit cycle oscillation and can be differentiated from other types of self-sustained oscillations by its limited amplitude. Limit cycle oscillations occur due to the existence of nonlinear properties in the fluid-structure interaction of the aeroelastic system. In stall flutter, the nonlinearity is due to the dynamic stall phenomenon. In a recent paper, Dimitriadis and Li [10] showed experimentally that this particular nonlinearity can lead to complex bifurcation behavior, such as subcritical Hopf bifurcations. Furthermore, its interaction with static divergence can cause a saddle connection bifurcation, resulting in asymmetric LCOs, even when the wing is symmetric and its static angle of attack is zero. Finally, the experiments showed that the interaction between these two instabilities can lead to chaotic oscillations.

Dimitriadis and Li [10] used a pitch–plunge airfoil with high plunge stiffness and low pitch stiffness for their experiments. Therefore, the dynamics of the plunge degree of freedom did not participate in the oscillations they observed. Furthermore, all of the experiments they performed were for a static angle of attack equal to zero. The purpose of the present work is to carry out experiments on a wing that features close pitch and plunge natural frequencies and is therefore capable of undergoing classical pitch–plunge flutter. Then, by varying the static angle of attack, it is intended to investigate how stall flutter is generated and to determine its relationship to classical flutter. In addition to vibration and pressure measurements, particle image velocimetry (PIV) flow visualizations are performed around the midspan of the wing to provide a partial visualization of the flowfield. The main issue of interest is the observation of the mechanisms by which flutter evolves from a degenerate Hopf bifurcation (classical linear flutter) to a sub- or supercritical Hopf bifurcation (stall flutter).

II. Experimental Setup

A. Structural Setup

The experiments were conducted in the Multi-Disciplinary Low Speed Wind Tunnel of the University of Liège. The wind-tunnel features two working sections: one for aeronautical and automotive

Received 28 October 2010; revision received 9 February 2011; accepted for publication 15 February 2011.

*Researcher, Department of Aerospace and Mechanical Engineering, BAT: B52/3, chemin des Chevreuils, 1; nrazak@student.ulg.ac.be.

†Researcher, Department of Aerospace and Mechanical Engineering, BAT: B52/3, chemin des Chevreuils, 1; t.andrianne@ulg.ac.be.

‡Assistant Professor, Department of Aerospace and Mechanical Engineering, BAT: B52/3, chemin des Chevreuils, 1; gdimitriadis@ulg.ac.be. Senior Member AIAA.

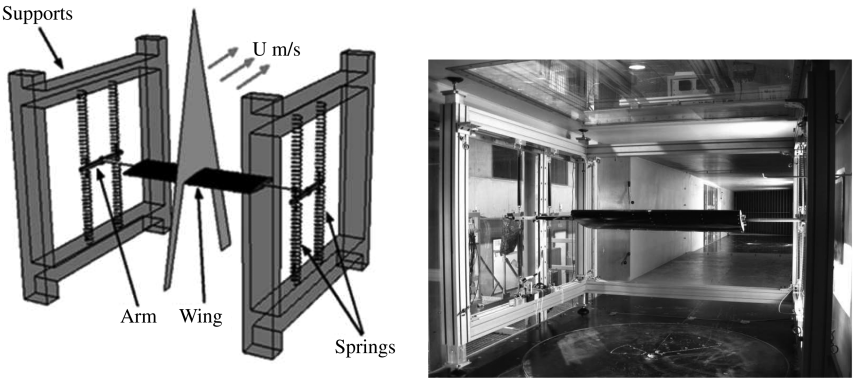

a) Drawing b) Photograph in wind tunnel

Fig. 1 Wing and support design and construction.

applications and one for wind engineering applications. The present experiments were carried out in the aeronautical working section, which has dimensions of $2 \times 1.5 \times 5$ m (width by height by length) and is capable of achieving airspeeds of up to 60 m/s in the tunnels closed-loop configuration. The turbulence level is 0.15% on average at the lower speed range. For the stall-flutter experiments a special support framework was assembled, which was used to fix extension springs. The other ends of the springs were fixed to arms that act as adaptors to the wing spar. The spar is connected to the center of the arm. Free play is avoided by securely attaching the spar to the adaptor arms. The suspension springs allow movement in all directions. The support mechanism described was designed to allow frictionless wing vibrations with known structural stiffness values. Eight to 16 springs can be installed to suspend the wing and keep it in tension. Even numbers of springs were used to ensure symmetry in stiffness. The support structure was sufficiently far from the wingtips to not significantly affect the flow over the wing. The complete support system is shown in Fig. 1.

B. Wing

The rigid straight rectangular wing was made from aluminum and balsa wood. The chord was 36.0 cm long and the span was 100 cm, resulting in an aspect ratio of 2.78. The skin was made from a 0.5-mm-thick aluminum sheet that was wrapped around the balsa ribs. There were six ribs inside the wing, positioned 18.0 cm apart. The 2.0-cm-thick ribs were held together by an aluminum rod acting as a main spar, located at 37% of the chord. The profile selected for this study was the NACA 0018. This thickness ratio was chosen for two reasons: first, it was high enough to allow the installation of instrumentation inside the wing; second, it was thicker than the NACA 0012 profile investigated by Dimitriadis and Li [10]. It was hoped that the increased thickness would give rise to different stall phenomena. The wing was designed to allow a ballast to be attached internally. The mass of the wing (including the main spar, adaptor arms, and instrumentation) was 6.47 kg, and the stiffness of the springs was 755 N/m. As the maximum instantaneous pitch angle of the wing obtained during the experiments was around 25°, the maximum instantaneous wind-tunnel blockage factor was 5%. Therefore, blockage phenomena had a negligible effect on the flow over the wing.

To measure the unsteady pressure distribution, 16 pressure tappings were drilled on the surface of the wing, at the midspan point. The tappings were connected to 16 piezoresistive pressure transducers [13] by means of plastic tubes. The pressure tappings were positioned symmetrically on the wing's upper and lower surfaces, as shown in Fig. 2.

The motion of the wing was measured using four accelerometers that were attached on the adaptor arms. Their frequency measurement range was 0–300 Hz with accuracy of ±5%, and their acceleration measurement range was ±50 g. For each wind-tunnel test the pressure sensors and accelerometers were sampled at 1.0 kHz over 4 s. The signals were acquired using a National Instruments (NI) PXI 1010 data-acquisition module managed by LabVIEW 9 software. From these measurements, the pitch and plunge displacements of the wing were reconstructed by numerically integrating the acceleration values twice. There were no end plates attached to the wingtips in order to allow a good quality of flow visualization; as a result, the flow over the wing was three-dimensional.

C. Particle Image Velocimetry

Time-resolved PIV was used to capture the instantaneous velocity field in a plane parallel to the freestream and perpendicular to the wing's chord during both steady responses and stall-flutter oscillations. The triangular laser plane is shown in Fig. 1a. Time-resolved PIV is an extension of the standard PIV technique described by Adrian [14], whereby images are acquired at a faster rate. The technique generates instantaneous velocity maps in a two-dimensional cross section of the flow. The spatial resolution and the accuracy of the measurement, if performed carefully, are considered to be high. The measured velocity vectors can then be used for a wide range of postprocessing calculations, including velocity magnitude and direction, velocity gradient, viscous shear, stream function, and vorticity [15]. This technique is important in the investigation of stall-dominated flow. Mean and fluctuating flow components can be calculated based on multiple realizations to represent the statistical parameters of unsteady aerodynamic flow.

The PIV investigation area for this work was chosen on the wing's upper surface, where six different positions along the mid span were interrogated. These six interrogation areas were chosen as a workaround to the inability of the PIV system to capture bigger observation areas. The interrogation areas were illuminated with a 527 nm, 2×10 mJ Litron double-pulse laser, producing a 10 ns pulse and a variable duration between pulses. The tunnel was seeded using a particle generator placed inside the wind tunnel. Since the wind tunnel was operated in closed-loop mode, seeding was turned off after some time to avoid speckle. Digital image sequences were acquired using a charge-coupled-device camera (Phantom V9.1, 1600×1200 pixels) mounted on a traversing system outside the test section.

The velocity vector field was calculated using the adaptive correlation function in the standard two-dimensional PIV software

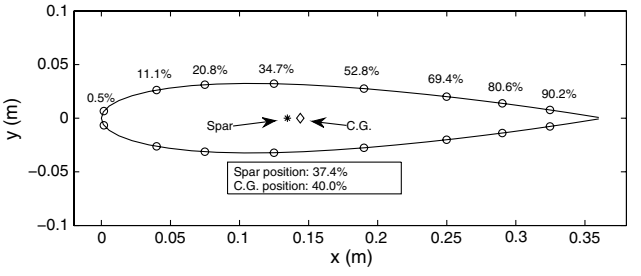

Fig. 2 Position of pressure sensors, spar and center of gravity relative to the wing section.

system supplied by Dantec Dynamics (Dynamic Studio). The interrogation area used for analysis was 64×64 pixels with a 50% overlap and a validation area that included subpixel interrogation to improve accuracy. All further processing was carried out in MATLAB software. The first image captured during the oscillation was manually triggered in the PIV software. All subsequent images were triggered via preset time stepping. The trigger signal was also captured by the NI data-acquisition system, which launched the simultaneous pressure and acceleration data acquisition. For all cases, 500 image pairs were sampled over 1 s.

III. Test Description

The experiments for this work were divided into two series. The first series of tests involved measurements of the pressure and acceleration data only. This series of tests is used to determine the speed ranges at which stall flutter occurs and the corresponding oscillation amplitudes and frequencies. From the aerodynamic perspective, the pressure measurements provided the flow properties around the midspan section of the wing. Sectional lift and moment coefficients were computed to give an insight into the flow-separation mechanism experienced by the wing. This series of tests was conducted at different airspeeds, U, and static angles of attacks, α_0. The static angle of attack is the static equilibrium position of the wing before being exposed to the airflow. It was set by changing the angle at which the wing spar was fixed to the adaptor arms and was measured using a digital inclinometer. The chosen static angles of attack were 11, 12, 13, 14, and 16°, and they were set by means of a digital inclinometer. The airspeed was varied between 8 and 25.2 m/s. Since stall-flutter oscillations are self-excited, no external excitation of the structure was necessary.

The second series of tests included PIV measurements as well as pressure and acceleration data collection. This series of tests was designed to provide further insight into the stalled flowfield. PIV data were used to correlate to the results obtained from the first series of tests. Separation and vortices were visualized and characterized using PIV-generated velocity vectors maps. The tests of the second series only looked at specific airspeeds and angles of attack, i.e., $\alpha_0 = 13$ and 16° with airspeeds between 12.0 and 18.0 m/s. The Reynolds number range employed in this work was between 2.6×10^5 and 6.3×10^5.

The wing's dynamic response was measured and analyzed at wind-off conditions using hammer testing. Several hammer impulses were applied to different points on the wing and the accelerometer responses were recorded and processed. The impulses were applied on the leading and trailing edges to induce mainly pitching motion, on the wing spar to induce mainly plunging motion, and in intermediate positions to induce combined motion.

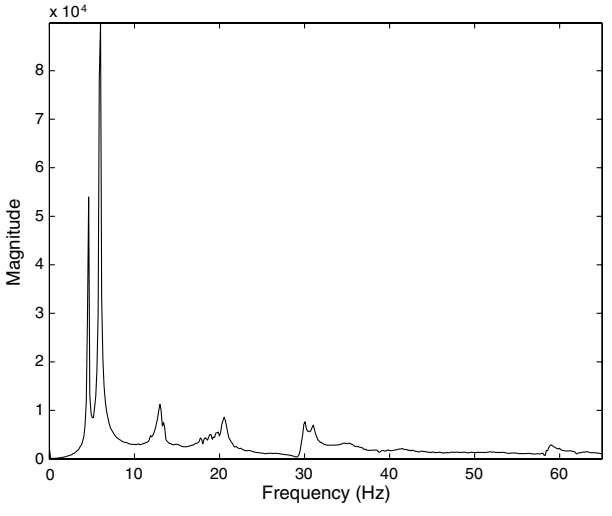

Fig. 3 Fourier transform of accelerometer 1 response at $U = 0$ m/s.

Table 1 Modal frequencies and damping ratios at $U = 0$ m/s

Mode	Frequency	Damping ratio
Plunge	4.57 Hz	0.0033
Pitch	5.95 Hz	0.0087
Roll	13.10 Hz	0.0418

The time responses were Fourier-transformed and averaged in order to obtain the impulse responses of the system. Figure 3 shows the magnitude of the averaged Fourier transform of the accelerometer 3 responses between 0 and 60 Hz. It can be seen that there are three major frequency components at 4.6, 6.0, and 13.0 Hz. These correspond to the plunge, pitch, and roll degrees of freedom, respectively. There are three further frequency components at 20.6, 30.1, and 59.0 Hz. These correspond to the other three degrees of freedom of the wing: i.e., yaw, spanwise motion, and chordwise motion.

The measured responses were curve-fitted using a rational fraction polynomial (RFP) [16] approach in order to more accurately estimate the modal parameters of the wing at wind-off conditions. The results are tabulated in Table 1. Only the plunge, pitch, and roll results are presented; none of the accelerometers were oriented in the in-plane direction, and therefore the modal parameters identified for the in-plane modes are untrustworthy.

IV. Dynamic Behavior

In this section the dynamic response of the wing during the wind-tunnel tests is described. The description and discussion is based mainly on the acceleration measurements. Each steady angle of attack is treated separately, starting from 11° and going up to 16°. The pressure and PIV data are presented in later sections.

A. Angle of Attack of 11°

The responses observed for this angle of attack can be characterized as a classical flutter event. The wind-tunnel speed was increased from 22.5 to 25.5 m/s. Up to 25.1 m/s, the responses were of low-amplitude and random in nature, consistent with an aeroelastic system that is excited by the turbulence in the wind tunnel. The top plot of Fig. 4 shows a sample acceleration signal measured at 25.5 m/s to demonstrate this type of response. At 25.2 m/s, the nature of the response changed radically, leading to very-high-amplitude oscillations. A test was also carried out at 25.5 m/s and the response amplitudes were even higher. The bottom plot of Fig. 4 shows an acceleration signal from the 25.2 m/s test, showing that there is a clear difference in both amplitude and form between the signals measured at pre- and postcritical conditions. It can be seen that the acceleration amplitude increases with time in the postcritical condition; the test was stopped when the acceleration exceeded 40 g. There was no damage to the wing. The next test at $U = 25.5$ m/s revealed that the vibration amplitude stabilizes itself at 100 g, which is beyond the measurement range of the accelerometers. This was a particularly dangerous vibration and no further tests were carried out at this, or any higher, airspeed.

The power spectral density (PSD) of the accelerometer signals were calculated using Welch's method. The PSD values at all airspeeds for accelerometer 4 are plotted in Fig. 5 against airspeed, in the form of a contour plot. The bright areas denote a high value of the PSD. Frequencies up to 40 Hz are included in the plot. It can be seen that as the airspeed is increased, the plunge and pitch frequency components (4.6 and 6 Hz, respectively, at $U = 0$ m/s) approach each other. At airspeeds higher than 25 m/s only one frequency component is visible, at 5.9 Hz. This phenomenon appears to be a classical pitch–plunge flutter mechanism.

As no external excitation was applied to the wing, apart from the natural turbulence of the wind-tunnel, input–output modal analysis methods could not be used to extract the modal parameters of the system and to verify the classical flutter conclusion. Assuming that

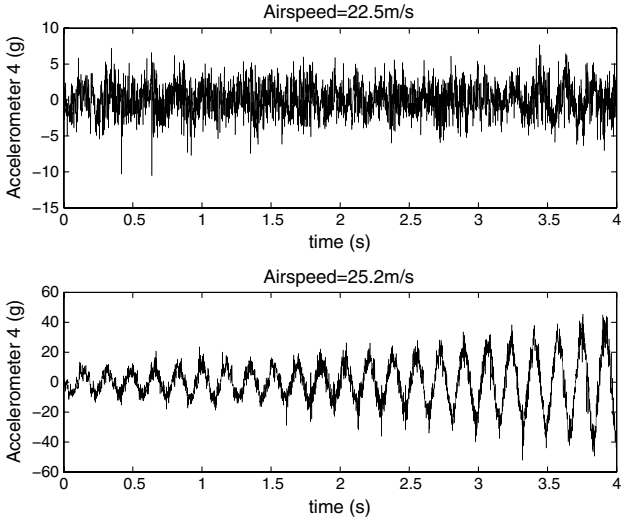

Fig. 4 Accelerometer responses at two different airspeeds for $\alpha_0 = 11°$.

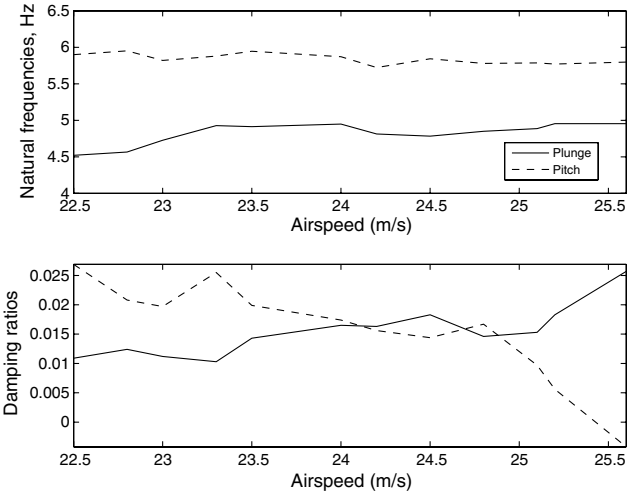

Fig. 6 Natural frequencies and damping ratios of the pitch and plunge degrees of freedom at all airspeeds for $\alpha_0 = 11°$.

the excitation was white noise, the Fourier transforms of the accelerometer responses were taken to represent frequency-response functions. In reality, the excitation is not white noise; however, the pressure sensor signals show that the spectrum of the pressures is reasonably flat up to a frequency of 10 Hz. Consequently, the rational fraction polynomial method was applied to the Fourier transforms of the accelerometer responses in order to estimate the modal parameters of the pitch and plunge degrees of freedom. The application of the RFP technique was localized in the 0–10 Hz range. Figure 6 plots the variation of the estimated natural frequencies and damping ratios with airspeed. It can be seen that as the airspeed is increased, the pitch damping ratio decreases to zero, whereas the plunge damping ratio increases. At the same time, the two natural frequencies approach each other, as indicated in Fig. 5.

Integrating the accelerometer signals twice allowed the estimation of the pitch and plunge displacement amplitudes. The integration was carried out in the time domain using a central-difference scheme, coupled with a bandpass filter between 2 and 80 Hz. Worden and Tomlinson [17] show that this approach yields good integrations when the filter is suitably chosen and applied.

The mean pitch amplitudes of the LCOs were estimated by separately averaging all the peaks and all the troughs of the pitch response signals. Figure 7 shows the response amplitude of the pitch degree of freedom at all the tested airspeeds for this angle of attack. The figure plots the mean of the peaks and troughs, together with error bars denoting the spread of the peak and trough values of the pitch response. It can be seen that the response amplitude is very small and has very low variability at all airspeeds up to and including 25.1 m/s. Very-high-amplitude oscillations with high variability appear abruptly at $U = 25.2$ m/s. Again, this behavior is consistent with a classical pitch–plunge flutter mechanism, occurring at 25.2 m/s. The large spread of the pitch amplitude in this speed range is due to the fact that the response is not periodic; its amplitude increases in time, as shown in the bottom plot of Fig. 4.

B. Angle of Attack of 12°

The wing's response at $\alpha_0 = 12°$ presents several significant differences with the response observed at $\alpha_0 = 11°$. Figure 8 shows the evolution of the response of accelerometer 2 at airspeeds between 20.5 and 21.5 m/s. At 20.5 m/s the response is low-amplitude and random in character. At 20.8 m/s however, there is a clear periodic component to the response, even though the amplitude is still low, of the order of 5 g. At 21.2 m/s the response amplitude increases from about 8 to about 16 g over 4 s and then stabilizes itself. At even higher airspeeds, such as $U = 21.5$ m/s, the response is a limit cycle oscillation of significant amplitude. The highest airspeed that was tested was 25.2 m/s, where the acceleration response amplitude reached 80 g (beyond the linear range of the accelerometers).

Furthermore, the behavior of the response frequencies changes significantly in character with angle of attack. Figure 9 plots the amplitude of the PSD of the system responses against airspeed and should be compared with Fig. 5. It can be seen that the pitch and plunge frequency components are quite prominent, but appear to be

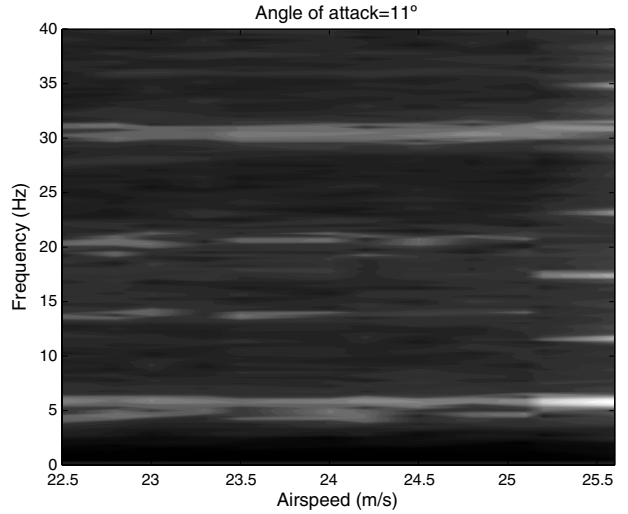

Fig. 5 PSD of accelerometer 4 at all airspeeds for $\alpha_0 = 11°$.

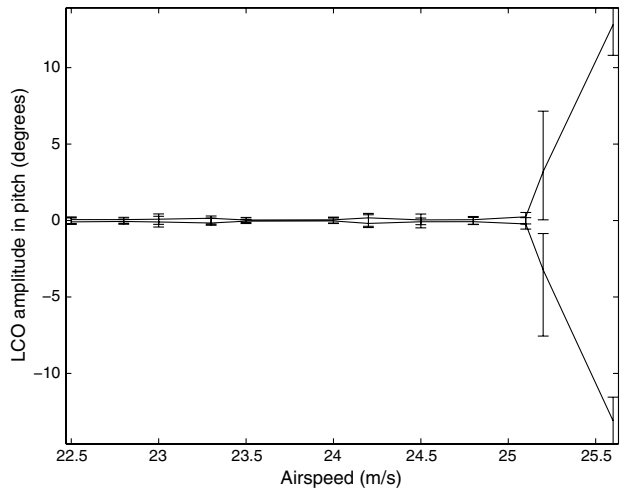

Fig. 7 Pitch response amplitude at all airspeeds for $\alpha_0 = 11°$.

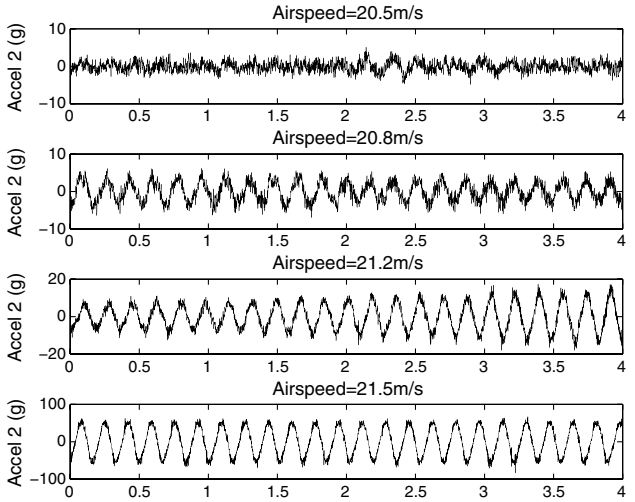

Fig. 8 Accelerometer responses at four different airspeeds for $\alpha_0 = 12°$.

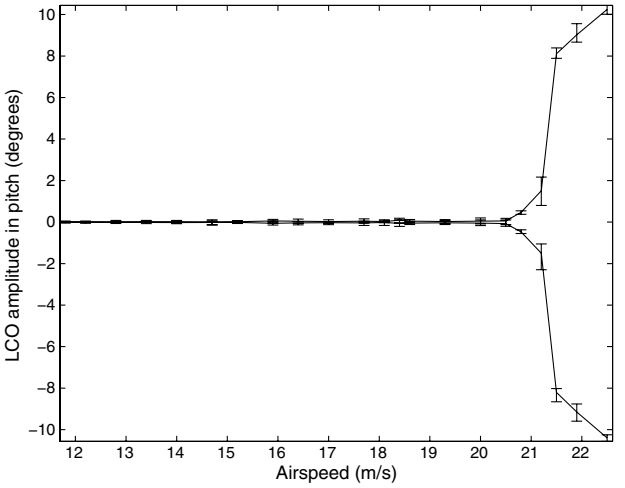

Fig. 10 Pitch response amplitude at all airspeeds for $\alpha_0 = 12°$.

largely unaffected by the airspeed and are not approaching each other, as in the $\alpha_0 = 11°$ case. Conversely, the frequency components that start at 15 and 30 Hz at $U = 12$ m/s increase linearly in frequency with airspeed up to $U = 21.2$ m/s, the airspeed at which the high-amplitude periodic responses were obtained.

It is clear that at high airspeeds the wing's response is characterized by very-high-amplitude LCOs. However, these oscillations appear less abruptly than in the $\alpha_0 = 11°$ case. At 20.8 m/s low-amplitude LCOs were observed and, even at higher airspeeds, the increase in amplitude is more gradual. The fact that the pitch and plunge frequencies do not approach each other is normal. This phenomenon should occur at airspeeds between 22 and 25 m/s, as demonstrated by the 11° results. The maximum airspeed tested for the present angle of attack was 22.5 m/s and there were already dangerous oscillations. Linear flutter is independent of the steady angle of attack, and the wing was not near linear flutter when the LCOs first appeared. Therefore, the mechanism that causes the oscillations at $\alpha_0 = 12°$ cannot be classical flutter; stall flutter is responsible, a fact that will be demonstrated with the PIV visualizations described later in this work.

Figure 10 shows the variation of the pitch response amplitude with airspeed. The graph demonstrates clear differences with the relevant plot for $\alpha_0 = 11°$ (Fig. 10). It can be seen that LCOs appear more gradually and at significantly lower airspeeds. There is an abrupt jump in LCO amplitude, but it occurs after LCOs have already appeared. It should be mentioned that the wind tunnel's speed controller is only sensitive to around 0.4–0.6 m/s at the speed range of the experiments presented here. Therefore, it was impossible to obtain a better airspeed resolution between 20.8 and 21.5 m/s, the airspeed range where the jump in amplitude occurs. Furthermore, the experiments were repeated with decreasing airspeeds and no hysteretic behavior was observed; the same LCO amplitudes were observed at the same airspeeds.

C. Angle of Attack of 13°

Significant qualitative and quantitative changes in the wing's responses were observed at this steady angle of attack. The first LCOs appear at 15.7 m/s, an airspeed markedly lower than the critical airspeeds of both the 11 and 12° cases. However, the most interesting aspect of the 13° angle responses is the appearance of hysteretic behavior. For this steady angle of attack the LCO amplitudes measured as the airspeed was increased are not equal to those measured when the airspeed was decreased.

Figure 11 shows the variation of the wing's pitch response amplitude with airspeed. As the airspeed was increased, LCOs of small amplitude were first encountered at 15.7 m/s. The amplitude increased slowly with airspeed up to and including $U = 17.2$ m/s. At 17.5 m/s the amplitude suddenly jumped to a much higher value. From there, the response amplitude continued to increase slowly up to 18.9 m/s, the maximum test airspeed.

When the airspeed was decreased, the LCO amplitude slowly decreased down to an airspeed of 16.8 m/s. At 16.5 m/s it jumped to a much lower value and, finally, the vibrations disappeared at 15.7 m/s. Figure 12 demonstrates this hysteretic behavior, showing

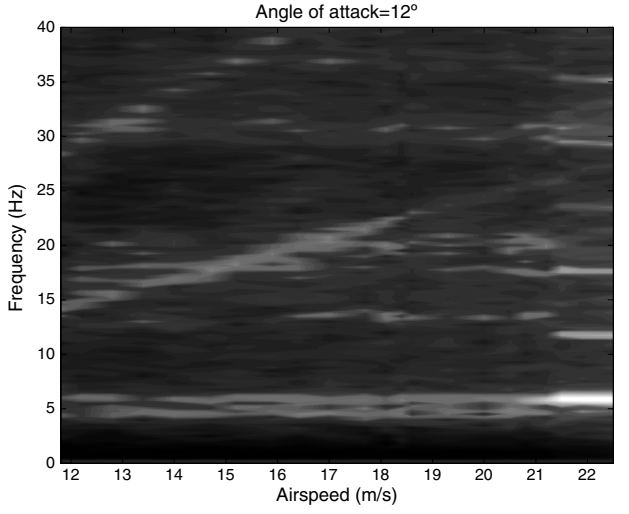

Fig. 9 PSD of accelerometer 2 at all airspeeds for $\alpha_0 = 12°$.

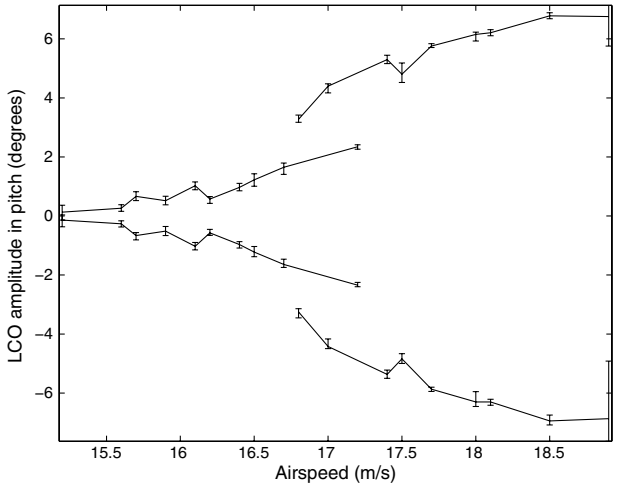

Fig. 11 Pitch response amplitude at all airspeeds for $\alpha_0 = 13°$.

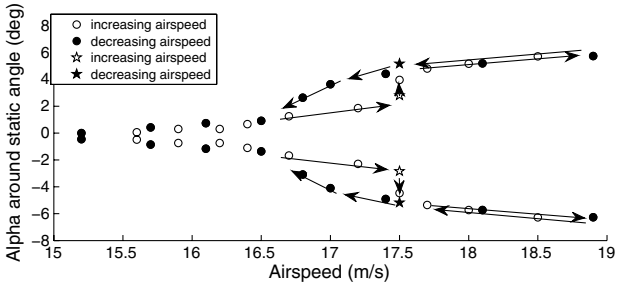

Fig. 12 Pitch response amplitude at all airspeeds for $\alpha_0 = 13°$, demonstrating hysteretic behavior.

the pitch amplitude variation with airspeed annotated with arrows that signal the direction of the airspeed variation.

Figures 11 and 12 demonstrate that there was an airspeed range between 16.7 and 17.4 m/s where two different values of the amplitude could be obtained, depending on whether the airspeed was increasing or decreasing. This jump phenomenon is characteristic of nonlinear systems undergoing a fold bifurcation and has already been encountered in aeroelastic systems undergoing stall flutter [10]. The LCO branch folds back on itself after 17.4 m/s and propagates in the decreasing airspeed direction as an unstable limit cycle. Just before 16.7 m/s the branch folds for the second time, becoming stable again and propagates in the increasing airspeed direction.

As already mentioned, fold bifurcations of limit cycles involve a change in the stability of the limit cycles [18]. A stable limit cycle becomes unstable after the fold and vice versa. As unstable limit cycles cannot be observed in practice, it is impossible to demonstrate formal proof of the occurrence of a fold bifurcation at this value of the static angle of attack. From a physical point of view, Fig. 11 shows that two different dynamic phenomena are possible and that they can overlap over a narrow rage of airspeed values.

The frequency content of the LCOs observed at this steady angle of attack are also of interest. Figure 13 plots the amplitude of the PSD of the combined accelerometer responses at all airspeeds. The dashed vertical line denotes the 15.7 m/s airspeed, i.e., the LCO onset condition. The two dash–dotted vertical lines denote the limits of the airspeed range in which two LCO amplitudes are possible. It can be seen that the low-amplitude LCOs contain both the pitch and plunge frequency components. Furthermore, they also include roll and other frequency components that increase with airspeed, as was the case at $\alpha_0 = 12°$. Conversely, the high-amplitude LCO features a fundamental frequency equal to that of the pitch degree of freedom and five harmonics in the 0–40 Hz range. It should be noted that for both

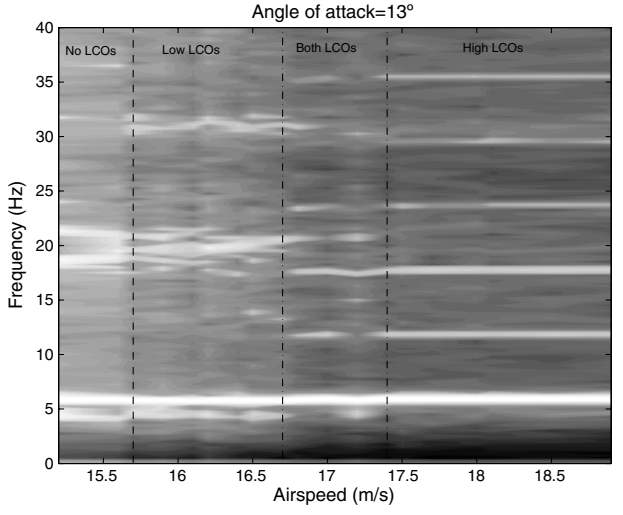

Fig. 13 PSD of combined accelerometer responses at all airspeeds for $\alpha_0 = 13°$.

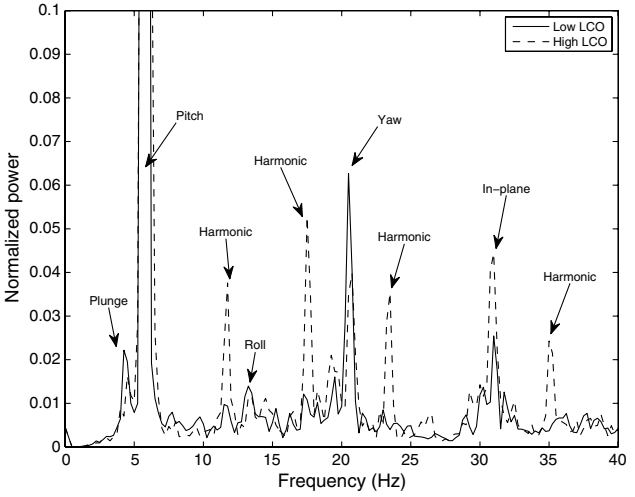

Fig. 14 Comparison between the frequency contents of low- and high-amplitude LCOs.

LCOs the most powerful frequency component is the pitch natural frequency. In the low-amplitude case the plunge natural frequency acts as a subharmonic.

To better demonstrate the differences between the frequency contents of the low- and high-amplitude LCOs, Fig. 14 plots the normalized PSDs of LCOs at $U = 16.7$ m/s (low-amplitude LCO) and $U = 16.8$ m/s (high-amplitude LCO). As already mentioned, in both cases the pitch frequency is the most important component, with the yaw coming a distant second. However, for the low-amplitude LCO the next two most important components are the plunge and the in-plane translation frequencies, whereas for the high-amplitude LCO the higher harmonics of the pitch frequency are more important.

The preponderance of higher harmonics in the high-amplitude LCOs suggests the existence of strong nonlinearity. Conversely, as the low-amplitude LCO does not feature any significant harmonics, it can be argued that it is the response of a linear system to harmonic excitation. Nevertheless, it should be noted that some harmonics are present in the low-amplitude responses, even though their power is low. Poirel et al. [19] presented a number of good arguments demonstrating that stall-flutter oscillations are self-sustained and not the result of harmonic aerodynamic forcing. One of these arguments concerns the Strouhal number of the measured oscillations. This number is defined as $Sr = fd/U$, where f is the frequency and d is the length of the wing's projection on a crossflow plane. The Strouhal numbers of all the LCOs observed during the present experiments ranged from 0.016 to 0.052 for a Reynolds number range between 2.6×10^5 and 6.3×10^5. Experimental measurements by Yarusevych et al. [20] demonstrate that the Strouhal of the vortex-shedding behind a NACA 0025 airfoil at 10° incidence and a Reynolds number of 2.3×10^5 is $Sr = 0.95$. Huang and Lin [21] measured the vortex-shedding frequency behind a cantilever rectangular wing with NACA 0012 profile and found that the Strouhal number is 0.2 at $Re = 1.25 \times 10^5$ and 15° incidence. Even taking into account the differences in the experimental parameters of these studies, the Strouhal number of the LCOs observed during the course of the present work is too low to be compared with the Strouhal of the vortex shedding behind a static airfoil. Therefore, neither the low-amplitude nor the high-amplitude LCOs can be the result of the application of an external excitation by the fluid; they must be self-sustained oscillations.

To better discuss the issue of the existence and degree of nonlinearity in the measured responses, consider a mathematical simplification of the complete aeroelastic system as a linear structural system excited by an aerodynamic excitation force, which can be periodic. When it is periodic, the excitation force contains a fundamental frequency and numerous harmonics, as it arises from a nonlinear aerodynamic phenomenon. The equations of motion of the structural system can be written as

$$\mathbf{M}\ddot{\mathbf{q}} + \mathbf{C}\dot{\mathbf{q}} + \mathbf{K}\mathbf{q} = \mathbf{f}(t) \tag{1}$$

where $\mathbf{M}$ is the structural mass matrix, $\mathbf{C}$ is the structural damping matrix, $\mathbf{K}$ is the structural stiffness matrix, $\mathbf{q}$ are the structure's generalized coordinates, and $\mathbf{f}(t)$ represent the aerodynamic excitation force. A Fourier series representation of this force can be written as

$$\mathbf{f}(t) = \sum_{k=1}^{\infty} \mathbf{f}_k \sin k\omega t + \mathbf{g}_k \cos k\omega t \tag{2}$$

where $\mathbf{f}_k$ and $\mathbf{g}_k$ are excitation amplitudes. If the excitation amplitudes are constants, then the structure's response is given by

$$\mathbf{q}(t) = \sum_{k=1}^{\infty} \mathbf{p}_k \sin k\omega t + \mathbf{q}_k \cos i\omega t \tag{3}$$

where $\mathbf{p}_k$ and $\mathbf{q}_k$ are response amplitudes calculated from

$$\begin{pmatrix} \mathbf{p}_k \\ \mathbf{q}_k \end{pmatrix} = \begin{pmatrix} -k^2\omega^2\mathbf{M} + \mathbf{K} & -k\omega\mathbf{C} \\ k\omega\mathbf{C} & -k^2\omega^2\mathbf{M} \end{pmatrix}^{-1} \begin{pmatrix} \mathbf{f}_k \\ \mathbf{g}_k \end{pmatrix} \tag{4}$$

Such structural responses are obtained in the case of the high-amplitude LCOs, containing frequency components only at the fundamental frequency and its harmonics. As the oscillations are self-excited, the excitation force must be related to the responses, i.e., $\mathbf{f}_k = \mathbf{f}_k(\mathbf{p}_k, \mathbf{q}_k)$ and $\mathbf{g}_k = \mathbf{g}_k(\mathbf{p}_k, \mathbf{q}_k)$.

Conversely, if the excitation amplitudes are not constants, but are functions of time, i.e., $\mathbf{f}_k(t)$ and $\mathbf{g}_k(t)$, then the structural response will contain the fundamental frequency and its harmonics, as well as transient responses at the system's natural frequencies. This appears to be the case for the low-amplitude LCOs; the measured responses contain frequency components at the natural frequencies and the response amplitude varies in time. The oscillations are still self-excited, but both excitation and response amplitudes are functions of time as well as of each other. Figure 15 plots the envelope function of the accelerometer 4 response at two airspeeds, 15.9 and 18 m/s. The first airspeed results in a low-amplitude LCO, whereas the second airspeed gives rise to a high-amplitude LCO. The two envelope functions were smoothed by applying a moving average procedure to remove high-frequency noise and normalized to unity. It can be clearly seen that there is significantly higher variability in the envelope function of the low-amplitude LCO, as the amplitude of the acceleration response varies in time from 0.6 to 1.

The unsteadiness in the amplitude of the low-amplitude LCOs reinforces the assertion made earlier that there are two distinct dynamic phenomena occurring at this value of the static angle of attack. Later in this work, it will be shown that all LCOs are due to the occurrence of periodic stall over the upper surface of the wing.

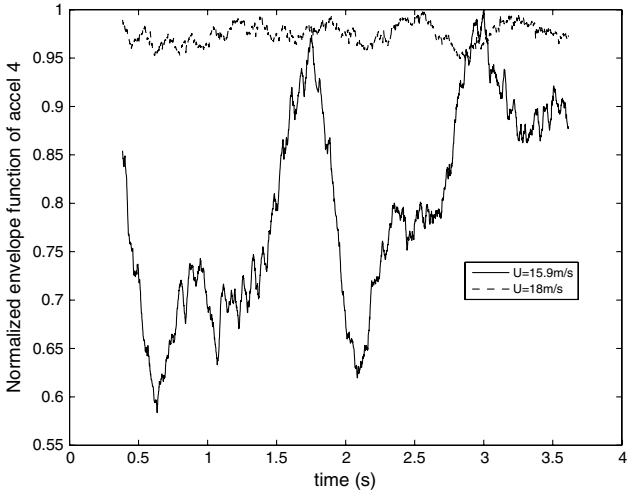

Fig. 15 Normalized envelope function of accelerometer response at two airspeeds for $\alpha_0 = 13°$.

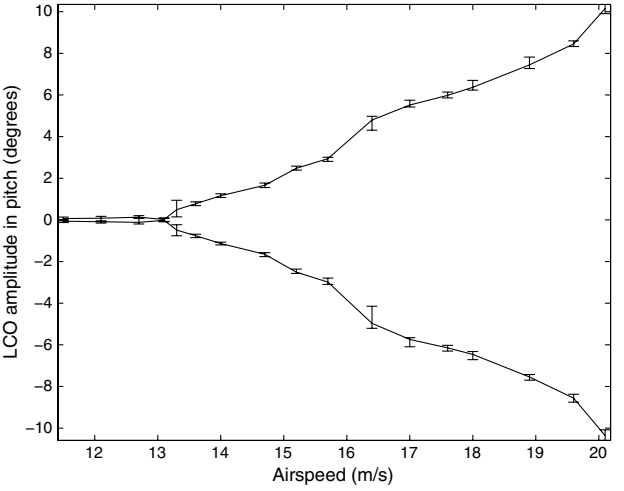

Fig. 16 Pitch response amplitude at all airspeeds for $\alpha_0 = 14°$.

However, the mechanism of the stall is different for different limit cycle amplitudes. The increased variability in the low-amplitude LCOs is due to the particular stall mechanism that causes such oscillations.

D. Angle of Attack of 14°

Low- and high-amplitude limit cycle oscillations were also observed at this steady angle of attack. The main differences with the 13° case are the airspeeds at which the LCOs occur and the fact that there appears to be no hysteretic behavior of the LCO amplitude and hence no fold in the LCO branch. Figure 16 shows the variation of the pitch response amplitude with airspeed for $\alpha_0 = 14°$. It can be seen that the first LCOs occur at an airspeed of 13.3 m/s and have low amplitudes. As the airspeed increases, the response amplitude increases steadily until, at $U = 16.4$ m/s, it jumps suddenly to a significantly higher value.

This particular steady angle of attack is very useful in investigating the effect of the LCO amplitude on its frequency content, since the amplitude increases to a significant value in a much more gradual manner than in the $\alpha_0 = 13°$. Figure 17 plots the PSD of the combined accelerometer responses at all airspeeds. The two horizontal dashed lines denote the LCO onset airspeed and the amplitude jump airspeed. It can be seen that the frequency content of the high-amplitude LCOs exclusively features the fundamental frequency of 6 Hz and its harmonics. Conversely, the LCOs that occur just after the onset speed contain several frequency components of the linear systems, such as the plunge and roll. However, this

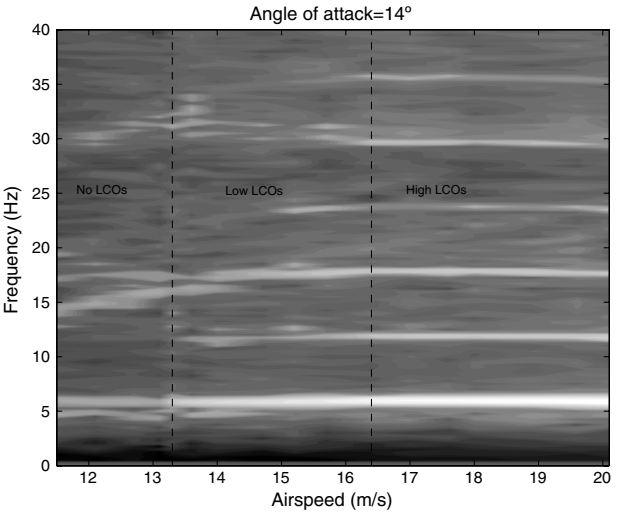

Fig. 17 PSD of combined accelerometer responses at all airspeeds for $\alpha_0 = 14°$.

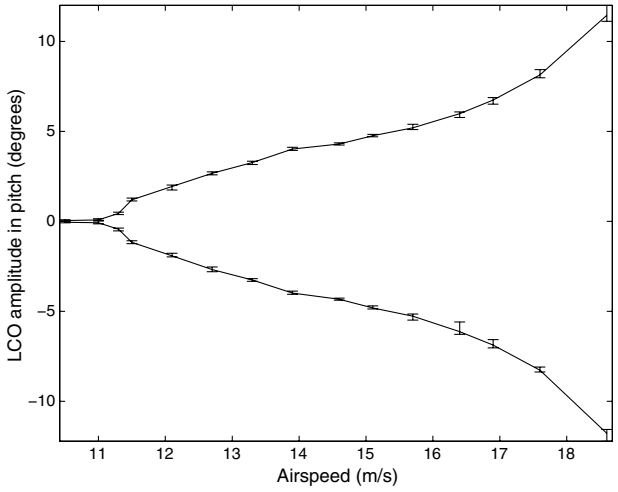

Fig. 18 Pitch response amplitude at all airspeeds for $\alpha_0 = 16°$.

time the harmonics of the fundamental frequency gradually start to become important before the jump, at an airspeed of around 15 m/s. At airspeeds higher than that the linear system modes start to disappear. Furthermore, the roll frequency (15 Hz at 12 m/s) increases steadily with airspeed until it seems to join the second harmonic at 18 Hz.

In general, the responses measured at $\alpha_0 = 14°$ are similar to those observed at $\alpha_0 = 13°$ in the sense that there are two distinct dynamic phenomena occurring at different airspeeds and giving rise to LCOs of different amplitudes and frequency contents. However, these two phenomena appear to gradually merge into each other at 14°, whereas in the $\alpha_0 = 13°$ case they are quite distinct.

E. Angle of Attack of 16°

At this static angle of attack LCOs first appear at 11.5 m/s. Their amplitude increases steadily with airspeed up to the maximum test airspeed of 18.6 m/s. There are no sudden jumps in amplitude. Figure 18 shows the pitch-angle response amplitude variation with airspeed. It is clear that the amplitude curve does not contain significant discontinuities, either in value or in slope. At airspeeds between 11.5 and 13.5 m/s the LCO amplitude is time-varying; at higher airspeeds the amplitude is stabilized.

Figure 19 shows the evolution of the frequency content of the responses with airspeed. It is clear that the dominant frequency components are the pitch frequency and its harmonics at airspeeds higher than 14 m/s. The plunge natural frequency is visible up to 13.5 m/s, and the roll frequency is apparent up to 14 m/s. As in the $\alpha_0 = 14°$, the roll frequency appears to increase with airspeed until it merges with the second pitch harmonic at 18 Hz.

Figures 18 and 19 demonstrate that at $\alpha_0 = 16°$ the phenomenon giving rise to the LCOs with unsteady amplitude is limited to airspeeds immediately after the critical flight condition. Furthermore, the passage from low-amplitude and time-varying to high-amplitude and steady LCOs is continuous, without any sudden jumps. At higher static angles of attack, the airspeed range at which low-amplitude LCOs are obtained is further reduced, but this is only a quantitative, not a qualitative, difference with the phenomena observed at $\alpha_0 = 16°$.

V. Description of the Bifurcation

In all the tests presented here, four types of responses were observed:

1) Random responses were the responses of the system to excitation by the natural turbulence of the tunnel and had very small amplitudes. These responses will be referred to as steady.

2) Low-amplitude limit cycle oscillations were self-excited responses with time-varying amplitude.

3) High-amplitude limit cycle oscillations were self-excited responses with steady amplitude.

4) Diverging oscillations were self-excited responses with rapidly increasing amplitude. They eventually led to very-high-amplitude LCOs, but their violence was such that the tests were interrupted for safety reasons. These oscillations will be referred to as *classical flutter*.

A bifurcation is the intersection of two or more of a system's solution branches. The intersection of a branch of steady solutions with a branch of dynamic solutions is usually called a Hopf bifurcation. As such an intersection clearly occurs in the experiments presented here, it can be safely said that the wing undergoes a Hopf bifurcation. There are two parameters governing this bifurcation: airspeed and static angle of attack.

Figure 20 shows the variation of the pitch-angle response amplitude with airspeed for all the tested angles of attack. The pitch angles were centered around zero by removing the value of the static angle of attack. The 11° line shows a typical classical flutter event; the response is steady until, at a critical flight condition, it suddenly becomes oscillatory with enormous amplitude. This phenomenon is known mathematically as a *degenerate Hopf bifurcation* [22]. Its degeneracy lies in the fact that at the critical condition there is no limit cycle, but an infinite number of neutrally stable circles.

An increase of 1° in the static angle of attack brings about a significant change in the bifurcation condition. The critical airspeed is lower, but, crucially, the postcritical behavior is totally different. The amplitude no longer tends to infinity, but it is finite and increases

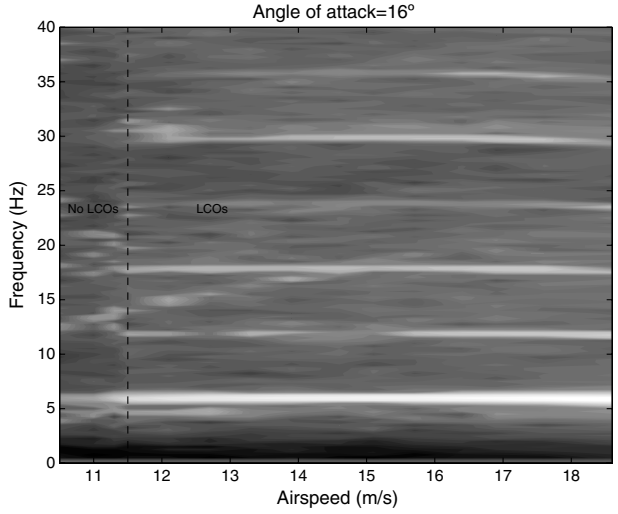

Fig. 19 PSD of combined accelerometer responses at all airspeeds for $\alpha_0 = 16°$.

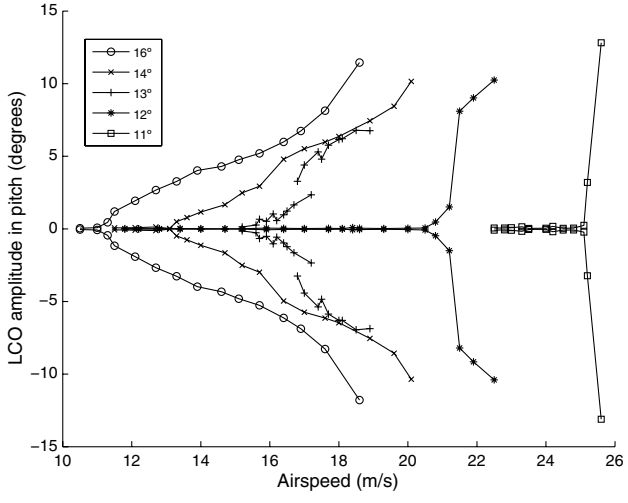

Fig. 20 Pitch response amplitudes at all angles of attack and airspeeds.

with airspeed. The degenerate Hopf has been transformed into a normal supercritical Hopf bifurcation. The LCO amplitude is initially low, but very quickly jumps to a very high value. This jump can come about as the result of a fold bifurcation, occurring shortly after the Hopf.

At 13° the critical airspeed has dropped even further. After the Hopf bifurcation there is now a significant airspeed range where low-amplitude LCOs can be encountered, followed by a fold and a jump to higher amplitude LCOs. The geometry of the fold is such that there exists an airspeed range in which the wing can undergo two different limit cycle oscillations.

At 14° the critical airspeed drops again. As in the 12 and 13° cases the Hopf is followed by a fold and a jump in amplitude. However, the jump is much smaller and an airspeed range in which two LCOs are possible was not identified.

Finally, at 16°, the critical airspeed has dropped to less than half the flutter speed at 11°. Furthermore, the fold bifurcation has disappeared. In summary, an increase of 5° in the static angle of attack transforms the degenerate Hopf bifurcation into a well-behaved supercritical Hopf bifurcation without any folds or other secondary phenomena.

VI. Aerodynamic Forces

As already mentioned, the bifurcation phenomena observed during these experiments are driven by nonlinearity in the aerodynamic forces. The nonlinearity stems from the periodic separation of the flow around the wing, but can lead to different types of oscillations: 1) LCOs of low and time-varying amplitude and 2) LCOs of high and constant amplitude.

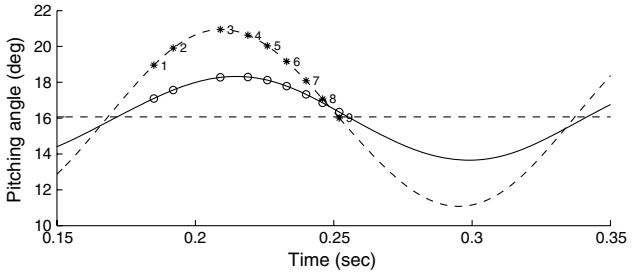

Fig. 21 Synchronized pitch-angle time signals at $U = 12$ m/s (solid line) and $U = 15$ m/s (dashed line) for $\alpha_0 = 16°$.

In this section the flow-separation phenomena occurring during these two types of LCO will be discussed, using the pressure and PIV measurements.

The experiments at $\alpha_0 = 16°$ were repeated with PIV measurements at two airspeeds, 12 and 15 m/s. The first airspeed leads to low-amplitude LCOs, and the second leads to high-amplitude LCOs. Pressure and acceleration were synchronously recorded. The PIV acquisition frequency was set to 500 Hz in all experiments. Typical pre- and postprocessing of the PIV images was applied in order to obtain the instantaneous velocity field. The size of each PIV window was 300 by 500 pixels, which is equivalent to 5.5 by 9.2 cm at the midspan position. A grid of 32 by 32 pixels was chosen to process the velocity field, resulting in a spatial resolution of 6 mm in both directions normal to the pitching axis of the wing. Clearly, the 5.5×9.2 cm window was too small to visualize the flow around the full wing section. Therefore, it was decided to carry out localized visualizations around the leading edge at several chordwise positions. All visualizations were centered on the midspan section of the wing.

The time duration of the measurements was set to 1 s, corresponding approximately to six cycles of the pitching oscillations. Figure 21 presents one of these cycles, where responses obtained from the two airspeeds have been synchronized with respect to the instantaneous pitching angle of the wing. In this figure, nine instances are selected in the first half of the cycle for further analysis. The velocity-field measurements revealed that the flow remains attached all over the wing's surface in the second part of the cycle, so these time instances are not discussed any further in this paper. A snapshot of the velocity field at the leading edge is taken at each time instance for both small and large oscillations. The nine pairs of snapshots are shown in Fig. 22.

In Fig. 22 the left plot at each time instance represents the $U = 12$ m/s case, and the right plot represents the $U = 15$ m/s case. The flow direction is represented by vectors; the dots are, in fact, very short vectors representing either very low local airspeed or zero airspeed. The thick solid line denotes the surface of the wing. Snapshot 1 ($t = 0.185$ s) shows attached flow everywhere on the surface of the leading edge (vectors) and no flow under the surface (dots). The same picture is seen in snapshot 2, except that for $U = 15$ m/s, there are some vectors that are not parallel to the

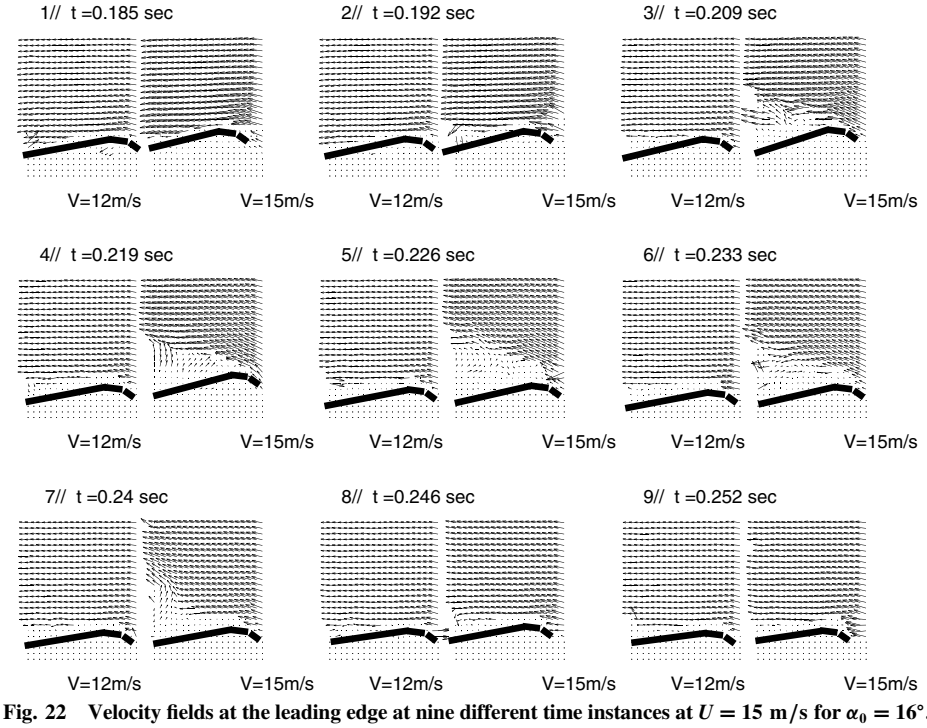

Fig. 22 Velocity fields at the leading edge at nine different time instances at $U = 15$ m/s for $\alpha_0 = 16°$.

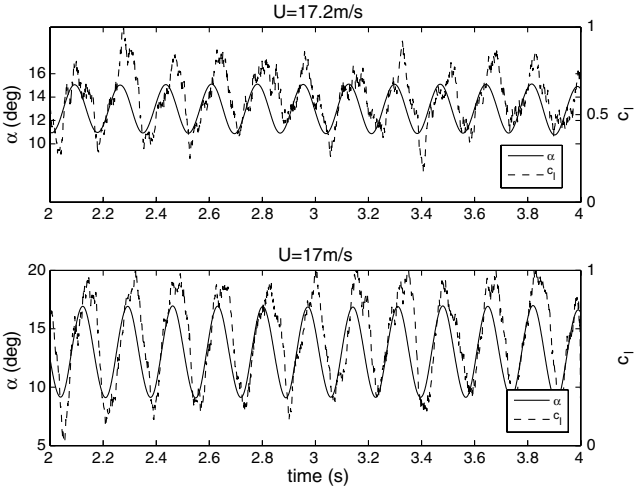

Fig. 23 Lift-coefficient variation at $\alpha_0 = 13°$ for low-amplitude LCOs (top) and high-amplitude LCOs (bottom).

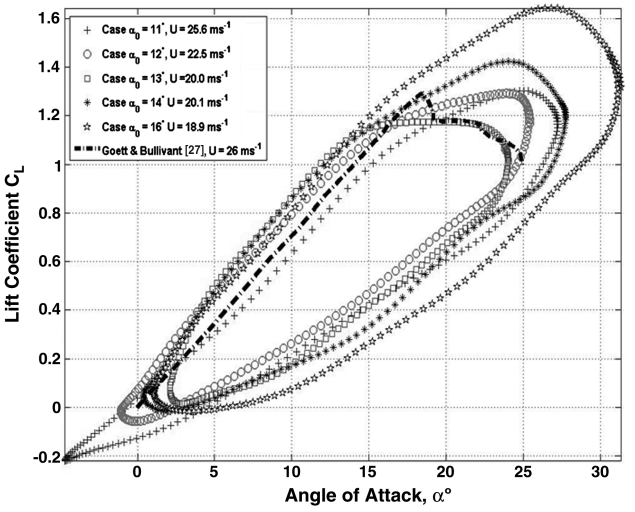

Fig. 24 Period-averaged lift-coefficient variation with pitch angle for high-amplitude LCOs at all airspeeds.

surface. In snapshots 3–7 the flow is completely separated at $U = 15$ m/s, but remains attached near the leading edge at $U = 12$ m/s. Finally, in snapshots 8–9 both flowfields are completely attached.

The vector fields of Fig. 22 demonstrate that there is a crucial difference between low-amplitude LCOs and high-amplitude LCOs: in the high-amplitude case the flow separation reaches the leading edge. Conversely, during low-amplitude LCOs the flow separation does not reach the leading edge. This difference can be used to explain the unsteadiness in the low-amplitude LCOs; the separation point is not well defined. At each cycle, the flow separates near the trailing edge and the separation point moves upstream. However, at each cycle the maximum travel distance of the separation point is different. Sometimes it reaches farther upstream than others, which causes an unsteadiness in the aerodynamic force variation with time and in the wing's response amplitude.

PIV observations of other LCOs confirmed the same behavior for the low-amplitude LCOs:

1) Flow separation begins in the rear half of the wing.

2) Flow separation propagates upstream during part of the cycle, but does not reach the leading edge.

3) The point furthest upstream that is reached by the separated flow varies from cycle to cycle.

In terms of the dynamic stall phenomenon, as described by McCroskey [23], the low-amplitude LCOs fall into the light stall category. This means that there is an area of separated flow over the rear part of the wing, but the flow near the leading edge remains attached.

Figure 23 plots the lift coefficient at the midspan position for $\alpha_0 = 13°$, calculated from integrating the pressure measurements around the wing section. The top plot concerns a low-amplitude LCO at $U = 17.2$ m/s and the bottom plot is a high-amplitude LCO at $U = 17.0$ m/s. The pitch (solid line) and lift-coefficient (dashed line) responses are plotted in both cases. It can be seen that both c_l responses display cycle-to-cycle variations. However, the variability of the lift during the low-amplitude LCOs is much more pronounced. These lift variations support the PIV observation that at low LCO amplitudes, the furthest upstream location of the separation point varies significantly from cycle to cycle. It is believed that this variability is causing the increased unsteadiness in the acceleration response of the wing, as seen in Fig. 15. Because the pressure measurements were carried out at the midspan point, they are therefore not representative of the full pressure distribution around the wing.

As far as the high-amplitude LCOs are concerned, it is clear from Fig. 22 that the flow-separation area reaches the leading edge at the midspan point. This stall phenomenon has been termed *deep stall* by McCroskey [23] and has been often associated with the shedding of a strong vortex at the leading edge [2,10,24–26]. This leading-edge vortex can significantly increase the maximum instantaneous lift, far beyond the steady maximum lift coefficient. Lift increases by up to a factor of 3 have been reported. However, Schreck and Helin [25] demonstrated experimentally that the effects of this vortex on 3-D wings are not as pronounced. In fact, they showed that this vortex is bow-shaped when seen from the top, as it is attached to the leading edge at the wingtips and curves downstream inboard, lying near the midchord point at the midspan point. Only the inboard section of the vortex separates from the surface of the wing and is shed in the wake.

The pressure measurements and PIV visualizations were used in an attempt to detect the presence of a leading-edge vortex during high-amplitude LCOs. The lift variations with time for the highest tested airspeed at each static angle of attack were period-averaged in order to smooth over the cycle-to-cycle variability. The resulting lift variations are plotted against instantaneous pitch angle in Fig. 24, along with the steady state lift curve for the NACA 0018 airfoil, as measured by Goett and Bullivant [27]. Between pitch angles of 0 and 18° the rising part of the lift curves is fairly close to the steady results. Beyond 18° there is an increase of the instantaneous lift coefficient, reaching a maximum of 1.65 for the $\alpha_0 = 16°$ case. Nevertheless, this maximum lift coefficient is far lower than the values reported from other experiments in cases of 2-D dynamic stall in the presence of a leading-edge vortex. Even the 3-D-wing dynamic stall experiments by Schreck and Helin [25] demonstrated maximum sectional lift coefficients starting at 2 and going up to 4 for a NACA 0015 wing. The small increase in maximum lift measured during the present experiments may suggest the absence of a leading-edge vortex or, at least, the presence of a weak leading-edge vortex. It should be stressed again that the results of Fig. 24 concern only the midspan position and not the full 3-D aerodynamics around the wing.

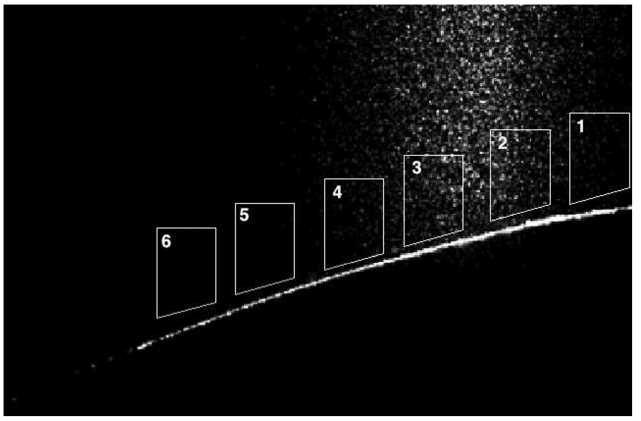

Fig. 25 Positions of PIV observation windows with respect to the wing's upper surface.

As the PIV visualization window was smaller than the wing's chord, it was not possible to observe simultaneously the flow over the entire surface of the wing. Therefore, the flow was observed at six different chordwise positions over several cycles, and the observations on each window were synchronized using the pitch-angle responses. Figure 25 shows the positions of these six PIV observation windows with respect to the wing's upper surface (white line). Each visualization window is termed a region of interest (ROI), with ROI 1 being nearest the leading edge and ROI 6 being nearest the trailing edge. The ROI covered 80% of the chord altogether.

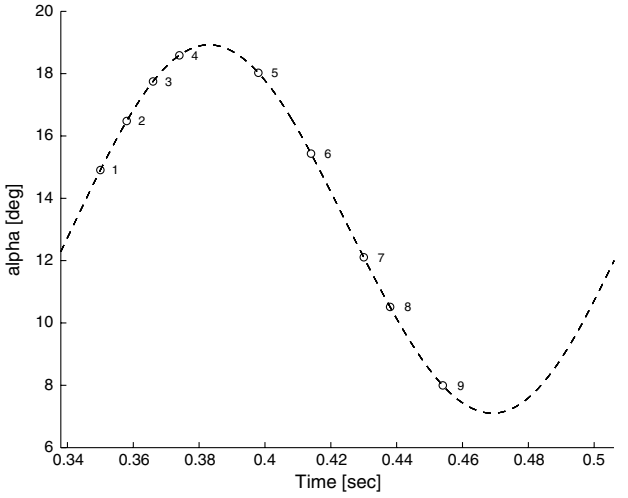

Fig. 26 Time instances at which the PIV snapshots are plotted on the three ROI.

The observations of the flowfield at $U = 17.5$ m/s and $\alpha_0 = 13°$ are examined in order to characterize the flow-separation phenomena occurring at the midspan point during high-amplitude LCOs. The flow visualizations are presented as snapshots at synchronized time instances of the flow in each of the ROI. The snapshots display both instantaneous velocity vectors and instantaneous vorticity contours. The exact time instances at which the snapshots are presented are shown with respect to the wing's pitch response in Fig. 26. The first snapshot is taken as the pitch angle is increasing and has a value of 15°, and the last is taken as the pitch angle is decreasing toward its minimum value.

Figures 27–29 present the snapshots of the flow in the ROI at the nine time instances. The dashed trapezoids denote the areas inside which the vorticity was calculated. Velocity vectors outside this area were not used in the vorticity calculations in order to avoid edge effects. The following observations can be made:

1) In time instance 1 (Fig. 27a), the velocity vectors are parallel to the surface and the vorticity is in general very low. In regions ROI 1 and ROI 2 there are areas of higher vorticity very near the surface.

2) In time instance 2 (Fig. 27b), the velocity vectors are still parallel to the surface and the vorticity is very low in ROI 4–6. However, in ROI 1–3 there are areas of higher vorticity near the surface.

3) In time instance 3 (Fig. 27c), there are areas of high vorticity and perturbations in the velocity vector directions near the surface in all the ROI. There appear to be two perturbed flow regions: one in the front half of the wing (ROI 1–3) and a separate one in the rear of the wing (ROI 4–6).

4) In time instance 4 (Fig. 28a), there are large areas of perturbed flow in all the ROI. These areas only cover about half the height of each window.

5) In time instance 5 (Fig. 28b), there are still large areas of perturbed flow in all the ROI. Over the rear part of the wing the

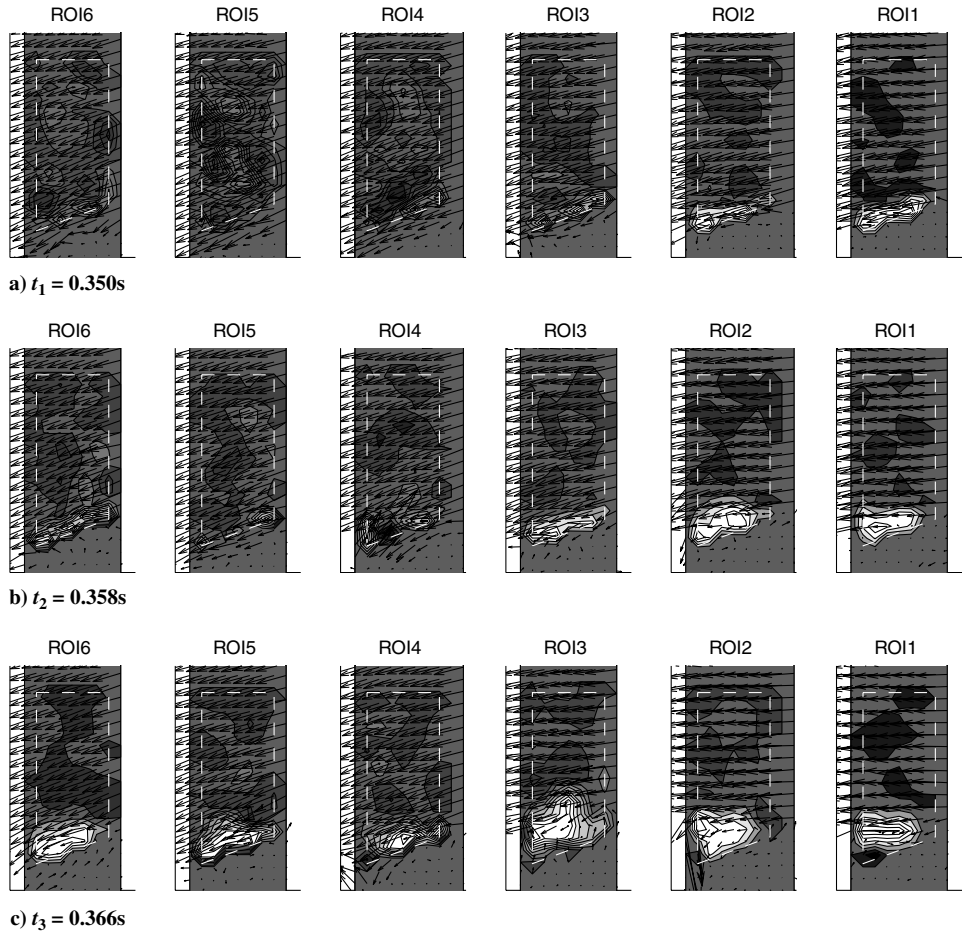

Fig. 27 Snapshots of the flowfield in the six ROI at time instances 1–3.

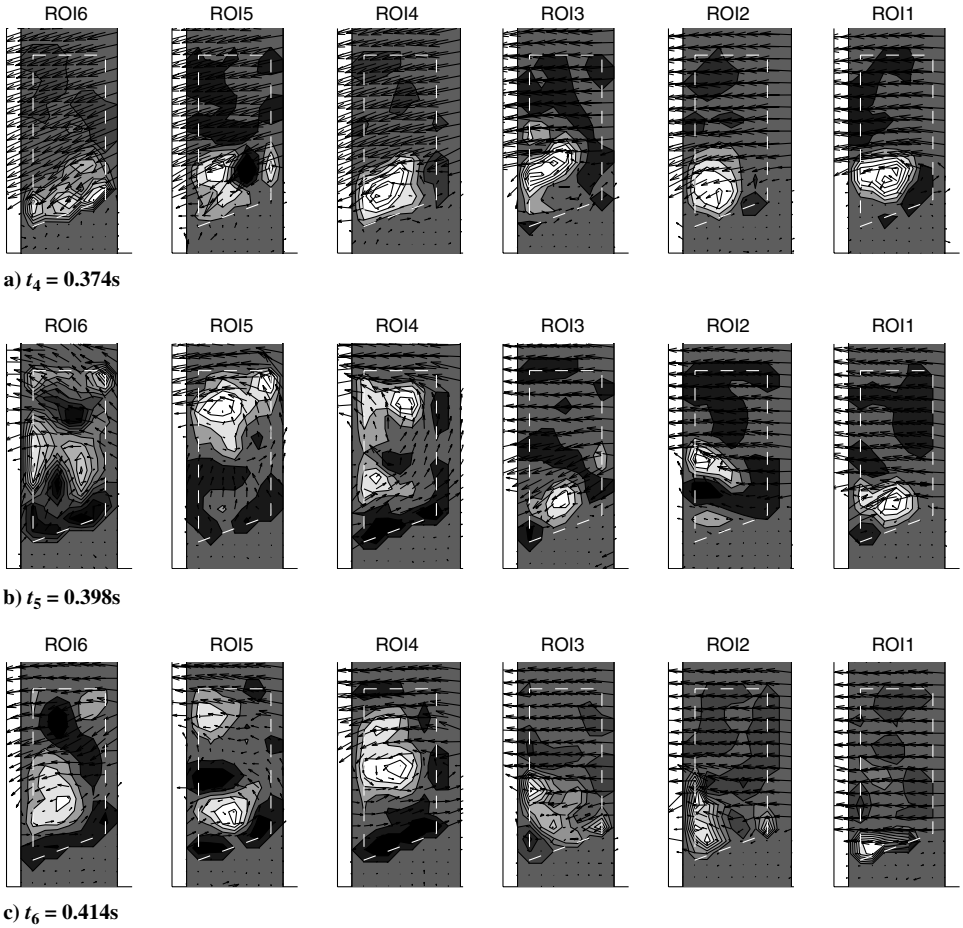

Fig. 28 Snapshots of the flowfield in the six ROI at time instances 4–6.

perturbed flow covers the entire height of the window, whereas over the front part of the wing it is still limited to the bottom half.

6) In time instance 6 (Fig. 28c), the flow perturbations start to disappear over the front half of the wing. The rear flow is still highly perturbed.

7) In time instance 7 (Fig. 29a), the flow is almost completely attached over the front half of the wing. The rear flow is still highly perturbed.

8) In time instance 8 (Fig. 29b), the flow is completely attached over the front half of the wing. The perturbations over the rear half are also much smaller in magnitude and area.

9) In time instance 9 (Fig. 29c), the flow is attached everywhere.

The observations of Figs. 27–29 shed a significant amount of light on the stall phenomenon. There appear to be two distinct regions of flow separation: one over the front half and one over the rear half of the wing. Leading-edge separation appears and disappears earlier and is contained inside the bottom half of the observation window. Trailing-edge separation appears and disappears later, but is much more violent.

As mentioned earlier, the deep stall phenomenon is often associated with the shedding of a powerful vortex, known as the leading-edge vortex. The discrete nature of the ROI means that even if there is a large and coherent leading-edge vortex, it cannot be observed in its entirety. Therefore, Figs. 27–29 cannot constitute proof of the existence or nonexistence of such a vortex. However, they do constitute proof of the fact that the leading-edge separation region is more contained than that of the trailing edge. The much higher extent of the separation region in ROI 4–6 in snapshots 28b to 29a may be an indication of the passage of a leading-edge vortex over the trailing edge. However, if there is really is a leading-edge vortex, its effect on the maximum lift coefficient is smaller than expected (see discussion of Fig. 24). This limited effect on the lift may be due to the fact that the vortex is ejected when the pitch angle is near its maximum and travels downstream far from the wing's surface. Looking at Fig. 28, if vortex shedding does take place, then it probably occurs between time instances 4 and 5, i.e., when pitch angle is at its maximum.

The existence of a region of flow separation near the leading edge of an airfoil is quite often related to the formation of a laminar separation bubble (LSB), which then bursts. LSBs occur at low-to-intermediate Reynolds numbers, such as those considered in the present work. Figure 27 could be described in such terms, if it is accepted that the higher-vorticity areas in ROI 1 and 2 form a separation bubble that spreads to ROI 3 and then bursts. However, it is not possible to confirm the existence of a LSB with the available data. It should be kept in mind that LSBs are generally associated with thin airfoils, although they have also been reported in dynamic stall and stall-flutter experiments for thicker airfoils with sharp leading edges [19,24].

VII. Conclusions

The high-amplitude LCOs observed during the course of the experiments presented in this work are characterized by an intriguing dynamic stall mechanism: separated flow first appears near the leading edge, followed by a distinct region of separation in the trailing edge. The classic deep stall phenomenon begins with trailing-edge separation; the formation of a leading-edge vortex and its shedding are subsequent events. The light stall phenomenon features only trailing-edge separation, which may or may not reach the leading edge. Finally, sharp-leading-edge stall features the creation of a laminar separation bubble near the leading edge that bursts and the shedding of the resulting leading-edge vortex. The stall type observed during the high-amplitude LCOs described here appears to be either a variant of deep stall or a combination of light stall and sharp-leading-edge stall.

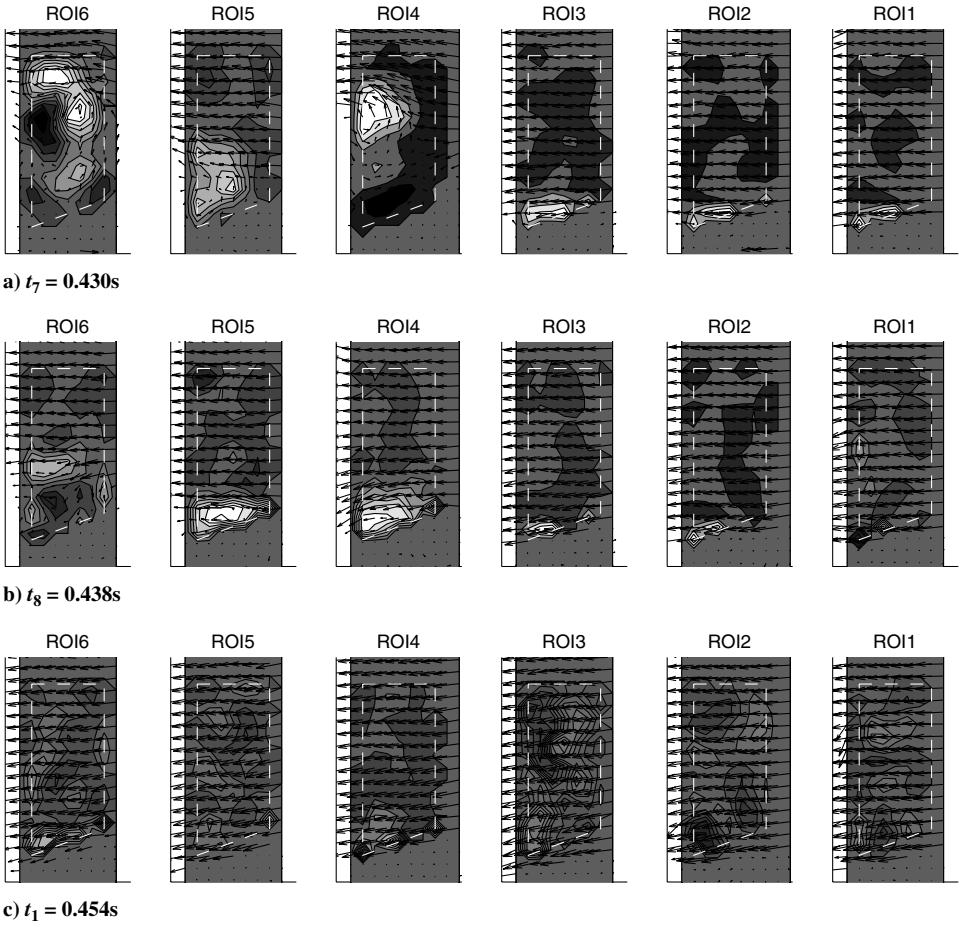

Fig. 29 Snapshots of the flowfield in the six ROI at time instances 7–9.

The NACA 0018 airfoil is quite thick, and trailing-edge separation should be expected to occur first. This is actually the case just after the supercritical Hopf bifurcation for all the angles of attack tested (apart from $\alpha_0 = 11^\circ$ where classical flutter occurred). However, the airfoil is also perfectly capable of leading-edge separation, as demonstrated by its dynamic stall mechanism at large LCO amplitudes. Nevertheless, it should be kept in mind that the experiments were carried out on a 3-D wing and, therefore, 3-D effects are expected to play a role in the observed phenomena. For example, in rectangular wings the leading-edge vortex always remains attached near the wingtips and only separates inboard.

The present experiments demonstrate that the dynamic stall mechanism plays a crucial role in the occurrence and characteristics of stall-flutter oscillations. However, the fundamental frequency of such oscillations remains unaffected by the stall mechanism or any of the aerodynamic parameters (angle of attack and airspeed); it is exclusively determined by the pitch natural frequency of the wind-off system. The critical mode in the classical flutter case (lowest static angle of attack) is the pitch mode. It can be concluded that flutter and stall flutter are related by the frequency of the critical mode, even though they are governed by different flow mechanisms.

References

[1] McCroskey, W. J., Carr, L. W., and McAlister, K. W., "Dynamic Stall Experiments on Oscillating Airfoils," *AIAA Journal*, Vol. 14, No. 1, 1976, pp. 57–63. doi:10.2514/3.61332

[2] Ericsson, L. E., and Reding, J. P., "Dynamic Stall at High Frequency and Large Amplitude," *Journal of Aircraft*, Vol. 17, No. 3, 1980, pp. 136–142. doi:10.2514/3.57884

[3] Spentzos, A., Barakos, G. N., Badcock, K. J., Richards, B. E., and Galbraith, R. A. M., "Computational Fluid Dynamics Study of Three-Dimensional Dynamic Stall of Various Planform Shapes," *Journal of Aircraft*, Vol. 44, No. 4, 2007, pp. 1118–1128. doi:10.2514/1.24331

[4] Ericsson, L. E., and Peter Reding, J., "Unsteady Airfoil Stall and Stall Flutter," NASA, CR 111906, 1971.

[5] Victory, M., "Flutter at High Incidence," Aeronautical Research Committee, Reports and Memoranda No. 2048, 1943.

[6] Bratt, J. B., and Wight, K. C., "The Effect Of Mean Incidence, Amplitude of Oscillation, Profile and Aspect Ratio on Pitching Moment Derivatives," Aeronautical Research Committee, Reports and Memoranda No. 2064, 1945.

[7] Halfman, R. L., Johnson, H. C., and Haley, S. M., "Evaluation of High-Angle-of-Attack Aerodynamic Derivative Data and Stall Flutter Prediction Techniques," NACA TN 2533, 1951.

[8] Rainey, A. G., "Some Observations on Stall Flutter and Buffeting," NACA RM L53E15, 1953.

[9] Dunn, P., and Dugundji, J., "Nonlinear Stall Flutter and Divergence Analysis of Cantilevered Graphite/Epoxy Wings," *AIAA Journal*, Vol. 30, No. 1, 1992, pp. 153–162. doi:10.2514/3.10895

[10] Dimitriadis, G., and Li, J., "Bifurcation Behavior of an Airfoil Undergoing Stall Flutter Oscillations in a Low Speed Wind Tunnel," *AIAA Journal*, Vol. 47, No. 11, 2009, pp. 2577–2596. doi:10.2514/1.39571

[11] Ham, N. D., and Young, M. I., "Limit Cycle Torsional Motion of Helicopter Blades due to Stall," *Journal of Sound and Vibration*, Vol. 4, No. 3, 1966, pp. 431–432. doi:10.1016/0022-460X(66)90138-6

[12] Fuykschot, P. H., and Kooi, J. W., "Stall Flutter of Sting-Supported Wind Tunnel Models," 27th AIAA Aerodynamic Measurement Technology and Ground Testing Conference, AIAA Paper 2004-2198, Portland, OR, July 2004.

[13] Li, J., and Dimitriadis, G., "Experimental Study of Stall Induced LCOS of Free-Vibrating Wings," *Proceedings of the CEAS International Forum on Aeroelasticity and Structural Dynamics*, Paper IF-026, Stockholm, June 2007.

[14] Adrian, R. J., "Particle-Imaging Techniques for Experimental Fluid Mechanics," *Annual Review of Fluid Mechanics*, Vol. 23, Jan. 1991,

pp. 261–304.
doi:10.1146/annurev.fl.23.010191.001401
[15] Gurka, R., Liberzon, A., Hefetz, D., Rubinstein, D., and Shavit, U., "Pressure Distribution using PIV Velocity Data," *3rd International Workshop on PIV'99*, Santa Barbara, CA, Sept. 1999, pp. 671–676.
[16] Richardson, M., and Formenti, D. L., "Parameter Estimation from Frequency Response Measurements Using Rational Fraction Polynomials," *Proceedings of the 1st International Modal Analysis Conference*, Orlando, FL, Nov. 1982.
[17] Worden, K., and Tomlinson, G. R., *Nonlinearity in Structural Dynamics*, Inst. of Physics, Philadelphia, 2001.
[18] Kuznetsov, Y. A., *Elements of Applied Bifurcation Theory*, Springer–Verlag, New York, 1998.
[19] Poirel, D., Harris, Y., and Benaissa, A., "Self-Sustained Aeroelastic Oscillations of a NACA 0012 Airfoil at Low-to-Moderate Reynolds Numbers," *Journal of Fluids and Structures*, Vol. 24, No. 5, 2008, pp. 700–719.
doi:10.1016/j.jfluidstructs.2007.11.005
[20] Yarusevych, S., Sullivan, P. E., and Kawall, J. G., "On Vortex Shedding from an Airfoil in Low-Reynolds-Number Flows," *Journal of Fluid Mechanics*, Vol. 632, 2009, pp. 245–271.
doi:10.1017/S0022112009007058
[21] Huang, R. F., and Lin, C. L., "Vortex Shedding and Shear Layer Instability of Wing a Low-Reynolds Numbers," *AIAA Journal*, Vol. 33, No. 8, 1995, pp. 1398–1403.
doi:10.2514/3.12561
[22] Strogatz, S. H., *Nonlinear Dynamics and Chaos: With Applications to Physics, Biology, Chemistry, and Engineering*, Perseus, Cambridge, MA, 1994.
[23] McCroskey, W. J., "The Phenomenon of Dynamic Stall," NASA TM 81264, 1981.
[24] McCroskey,W. J., and Philippe, J. J., "Unsteady Viscous Flow on Oscillating Airfoils," *AIAA Journal*, Vol. 13, No. 1, 1975, pp. 71–79.
doi:10.2514/3.49633
[25] Schreck, S. J., and Helin, H. E., "Unsteady Vortex Dynamics and Surface Pressure Topologies on a Finite Pitching Wing," *Journal of Aircraft*, Vol. 31, No. 4, 1994, pp. 899–907.
doi:10.2514/3.46577
[26] Lee, T., and Gerontakos, P., "Investigation of Flow over an Oscillating Airfoil," *Journal of Fluid Mechanics*, Vol. 512, 2004, pp. 313–341.
doi:10.1017/S0022112004009851
[27] Goett, H. J., and Bullivant, W. K., "Tests of NACA 009, 0012 and 0018 Airfoils in the Full-Scale Tunnel," NACA, Rept. 647, 1939.

E. Livne
Associate Editor